The BUB1 and BUBR1 paralogs scaffold the kinetochore corona

Verena Cmentowski[1,2*] & Andrea Musacchio[1,2*]

[1]Department of Mechanistic Cell Biology, Max Planck Institute of Molecular Physiology; Dortmund, 44227, Germany

[2]Centre for Medical Biotechnology, Faculty of Biology, University of Duisburg-Essen; Essen, 45141, Germany

*Corresponding authors. Email: verena.cmentowski@mpi-dortmund.mpg.de; andrea.musacchio@mpi-dortmund.mpg.de

Abstract

The kinetochore corona, a polymeric fibrous structure, facilitates chromosome biorientation and mitotic checkpoint signaling during mitosis. How its main building block, the RZZ complex, assembles on the outer kinetochore remains poorly understood. Harnessing corona biochemical reconstitutions and cell biology, we reveal the paralogous checkpoint proteins BUB1 and BUBR1 promote non-redundant branches of corona assembly. MPS1-kinase-dependent kinetochore docking of BUB1 and subsequent recruitment of BUBR1 initiates assembly. Disrupting the first branch by depleting CENP-E, a kinesin that links BUBR1 to RZZ, uncovered a second assembly pathway mediated by a direct interaction between BUB1 and ROD. Discovery of a direct interaction with the RZZ explains how the SAC protein MAD1 fits this corona assembly scheme. Our findings solve the long-standing puzzle of corona assembly and demonstrate the intimate interweaving of chromosome biorientation and checkpoint signaling.

Main Text

Introduction Kinetochores connect chromosomes to spindle microtubules and are essential for chromosome biorientation, mitotic fidelity, and genome stability (*1, 2*). Kinetochores are made of >80 different polypeptides with scaffolding and regulatory functions. The kinetochore corona is a crescent-shaped fibrous structure (*3*). It assembles beyond the KMN (Knl1 complex-Mis12 complex-Ndc80 complex), the main component of the microtubule-binding outer kinetochore layer. Early in mitosis, the corona transports chromosomes as cargoes towards the spindle equator using dynein-dynactin (DD) and CENP-E, microtubule motors of opposite polarity (*4*). Concomitantly, the corona promotes spindle assembly checkpoint (SAC) signaling by docking the MAD1:MAD2 complex (*3, 5*). When Ndc80C dependent end-on microtubule attachments replace motor-based lateral interactions, the corona disassembles, silencing the SAC and licensing sister

chromatin separation (*6-8*). CENP-E, the ROD-Zwilch-ZW10 (RZZ) complex, and the DD adaptor Spindly are the corona building blocks. Various outer kinetochore factors partially required for corona stability have been previously identified, but a comprehensive molecular view of corona assembly is missing. Using biochemical reconstitutions, electroporation of recombinant proteins, and separation of function mutants we now describe the entire corona assembly pathway. Our findings reveal that a complex of the paralogous SAC proteins BUB1 and BUBR1 initiates all interactions required for corona assembly. This resolves a long-standing question and underscores why chromosome biorientation and SAC signaling should be viewed as integrated and inseparable phenomena.

KNL1 scaffolds corona assembly Assembly of the corona into a fibrous meshwork arises from polymerization of the ROD-Zwilch-ZW10 (RZZ) complex, and also requires binding of Spindly to the RZZ (forming the RZZS complex) and MPS1 kinase-mediated phosphorylation of threonine 13 (T13) and serine 15 (S15) on the ROD subunit (*9-11*) (**Fig. 1A**). We have recently reported that when MPS1 kinase is inhibited with Reversine (*12*) to prevent RZZ polymerization, CENP-E becomes essential for kinetochore recruitment of RZZS (*13*). This, and additional evidence, identifies a previously unrecognized role of CENP-E in corona assembly and disassembly (*14-16*). Electroporation of the 812 kDa recombinant RZZ hexamer (tagged with mCherry) did not rescue corona assembly in cells depleted of CENP-E and treated with Reversine, but electroporation of the equivalent phosphomimetic T13E-S15E ($R^{EE}ZZ$) mutant complex did (**Fig. 1B**) (*13*). Thus, the corona assembles on at least another receptor in addition to CENP-E.

To identify the elusive receptor, we initially assessed how the outer kinetochore affects RZZ recruitment (see schematic in **Fig. 1C**). Simultaneous depletion of the Ndc80 complex (Ndc80C) and of KNL1 by RNAi (directed against multiple subunits in the case of Ndc80C, see Methods) eliminated RZZ entirely, while individual depletions of KNL1 or Ndc80C caused strong depletion, rather than elimination, of kinetochore-bound RZZ (**Fig. S1A-D**). These experiments implicate Ndc80C and KNL1 as being upstream of RZZ recruitment, but do not imply they have a direct role. First, Ndc80C and KNL1 sustain each other reciprocally at the kinetochore (quantified in **Fig. S1C-D**) (*17*). Second, each promotes recruitment of other proteins involved in RZZ recruitment (**Fig. 1C**). Specifically, Ndc80C is essential for kinetochore recruitment of MPS1 kinase (*18-21*), which promotes RZZS oligomerization (**Fig. 1A,C**). Conversely, KNL1 is necessary for recruitment of ZWINT (the second subunit of the Knl1C complex) and BUB1, which is itself MPS1-dependent (*10, 22-30*). Furthermore, BUB1 recruits the MAD1:MAD2 complex (also through MPS1), CENP-F, and BUBR1, whose pseudokinase domain promotes CENP-E recruitment, thereby indirectly contributing to localization of the RZZ complex to the kinetochore (**Fig. 1C**) (*13, 31*). Indeed, depletion of Ndc80C and KNL1 abrogated kinetochore localization of BUB1 and CENP-E in addition to RZZ (**Fig. S1E-F**).

Because mCherry-$R^{EE}ZZ$ localizes to kinetochores independently of CENP-E and MPS1 activity, monitoring its requirements for localization might enable us to close in on the RZZ receptor. We electroporated mCherry-$R^{EE}ZZ$ into cells depleted of either KNL1 or Ndc80C and monitored its

localization with and without MPS1 inhibition (**Fig. 1D**). As CENP-E is not required for mCherry-R^{EE}ZZ localization, we took the precaution of co-depleting CENP-E in these experiments to avoid possible confounding effects caused by its role in kinetochore recruitment of endogenous RZZ. Co-depletion of Ndc80C and CENP-E permitted substantial residual mCherry-R^{EE}ZZ localization (**Fig. 1E-G**). Further addition of Reversine eliminated residual mCherry-R^{EE}ZZ (**Fig. S1G-I),** indicating that elimination of Ndc80C exacerbates the consequences of MPS1 inhibition by Reversine, in line with the role of Ndc80C in recruiting MPS1 (*20, 21, 32*). As mCherry-R^{EE}ZZ bypasses MPS1 in RZZS polymerization, this observation suggests that MPS1 activity is required for an additional aspect of RZZS recruitment. Contrary to the co-depletion of Ndc80C and CENP-E, co-depletion of KNL1 and CENP-E prevented mCherry-R^{EE}ZZ recruitment very robustly, and further inhibition of MPS1 had only a minor additional effect (**Fig. 1E-G** and **Fig. S1G-I**).

Collectively, these experiments point to a crucial role of the KNL1 axis in RZZ recruitment, facilitated by MPS1 kinase activity. To identify regions of the 2316-residue KNL1 protein (isoform 2; **Fig. S2A**) relevant to RZZ recruitment, we depleted KNL1 and CENP-E and expressed different KNL1 constructs fused to an EGFP tag in stable DLD-1 cell lines (**Fig. 1H-I** and **Fig. S2C-G**). This analysis revealed that constructs containing at least one of the nineteen MELT (Met-Glu-Leu-Thr) motifs of KNL1 rescued recruitment of RZZ to kinetochores. As MELT motifs bind BUB1:BUB3 upon phosphorylation by MPS1 (*24, 27-31, 33, 34*) (**Fig. 1H** and **Fig. S2B**), this observation argues that BUB1, or a protein downstream of BUB1, contributes to kinetochore recruitment of RZZS in addition to allowing CENP-E recruitment through BUBR1.

To investigate this question, we depleted BUB1 (whose organization is schematically shown in **Fig. 2A**) by RNAi and assessed the impact on RZZ. In comparison to KNL1 depletion, which caused a very strong decrease of kinetochore RZZ, or to simultaneous depletion of CENP-E and BUB1, which completely removed RZZ from kinetochores (quantified in **Fig. 2B**), BUB1 knockdown only caused an incomplete depletion of RZZ from kinetochores (quantified in **Fig. 2B**). These results may seem inconsistent with the known epistatic relationships between the depleted proteins, as depletions of 1) KNL1, 2) BUB1, and 3) BUB1 and CENP-E ought to phenocopy each other with regard to RZZ recruitment (**Fig. 1C**). Nonetheless, previous studies investigating the involvement of BUB1 in RZZ recruitment have also yielded conflicting conclusions (*26, 35-41*), possibly due to incomplete depletions or ectopic interactions (as discussed in Conclusions). Thus, we opted to continue investigating whether BUB1, or of a protein downstream of BUB1, provides a platform for RZZ docking in addition to that provided by the BUBR1-CENP-E axis. Because CENP-E is dispensable for RZZ recruitment when RZZ forms polymers, we limited the analysis to the three proteins known to directly require BUB1 for kinetochore recruitment: CENP-F, BUBR1, and MAD1:MAD2. We have already shown that CENP-F is dispensable for RZZS recruitment (*42*). To test a CENP-E-independent role of BUBR1, we depleted BUB1 and replaced it with a BUB1 transgene lacking the BUBR1-binding region (Δ271-409) (**Fig. 2A**). This mutant continued to recruit RZZS (**Fig. 2C**), thus leaving only MAD1 or BUB1 itself as potential RZZ receptors.

BUB1 binds directly to RZZ The C-terminal domain of MAD1 ($MAD1^{CTD}$, residues 585-718) binds directly to residues 455-479 of BUB1 after phosphorylation of residues Ser459 and Thr461 by CDK1 and MPS1, respectively (**Fig. 2D**) (*43, 44*). Deletion of residues 437-521 of BUB1 encompassing this MAD1 binding site was also shown to reduce RZZ kinetochore levels (*36*). Previous evidence, discussed below, suggests that RZZ acts upstream of MAD1:MAD2 recruitment. Based on our new observations, we hypothesized that BUB1, by binding MAD1, may also facilitate RZZ recruitment. To test this, we first asked if we could reconstitute binding of MAD1:MAD2 to an immobilized GST-tagged fragment of BUB1 encompassing the previously identified binding region ($BUB1^{447-521}$). Indeed, both full-length MAD1:MAD2 and the $MAD1^{CTD}$ bound robustly to this fragment of BUB1 after *in vitro* phosphorylation with MPS1 and CDK1, and preventing phosphorylation abrogated binding (**Fig. 2E-F**, **Fig. S3A-D**, and **Fig. S5A-B**), in line with a previous report (*43*). In an unanticipated twist, a similar experiment using the same BUB1 bait and RZZ as the prey also revealed robust RZZ binding (**Fig. 2G-H** and **Fig. S3B-C**). We therefore reasoned that MAD1 and RZZ may bind concomitantly to different parts of the same BUB1 fragment. To test this, we titrated increasing amounts of $MAD1^{CTD}$ into a GST-BUB1 binding assay where RZZ was kept at a constant concentration. Contrary to our expectation, the amount of RZZ bound to BUB1 progressively decreased as $MAD1^{CTD}$ concentration increased (**Fig. S3B-D**). Thus, the $MAD1^{CTD}$ and RZZ bind competitively to an at least partly overlapping region of BUB1.

To clarify the molecular basis of this unanticipated competition, we dissected the BUB1:RZZ interaction in more detail. Within $BUB1^{437-521}$, an N-terminal α-helix between residues 465 and 475, coinciding with the ubiquitously conserved central domain 1 (CD1, also called CM1; residues 458-476), has been previously shown to interact with the $MAD1^{CTD}$ (*41, 43-47*). AlphaFold (*48*) predicts this N-terminal α-helix to be separated by an unstructured intervening region from a second α-helix between residues 498-507 (**Fig. 3B**). Residues in this second α-helix are only conserved in metazoans, to which RZZ is limited. We generated a series of N-terminal deletion constructs derived from $BUB1^{437-521}$ and tested them in solid-phase binding assays. For unclear reasons, $BUB1^{467-521}$ interacted with RZZ *in vitro* even more robustly than $BUB1^{437-521}$ (**Fig. 2G-H**). Truncation of ten additional amino acids ($BUB1^{477-521}$) strongly decreased the binding affinity to RZZ, though some residual binding was still observed relative to GST negative control. Any further deletions, including from the C-terminus, nearly eliminated RZZ binding (**Fig. S3E-F**). The robust binding of RZZ to $BUB1^{467-521}$ predicts that BUB1 phosphorylation is dispensable for this interaction. Indeed, phosphorylated and unphosphorylated $BUB1^{437-521}$ showed similar binding affinities for RZZ (**Fig. S5E-F**).

We introduced mutations in GST-$BUB1^{467-521}$ focussing on conserved and exposed residues (**Fig. 3A-B**). Mutating Phe475 to alanine strongly reduced RZZ (**Fig. S4A-B**). Mutating Phe500 and Glu501 ($467-521^{FE}$) reduced RZZ binding to background levels, as also did combining these mutations with Phe475 ($467-521^{FFE}$) (**Fig. S4A-B**). Also in analytical size-exclusion chromatography (SEC) experiments, where elution is determined by size and shape, all BUB1 constructs encompassing residues 467-521, including GST-$BUB1^{467-521}$ and GST-$BUB1^{209-521}$:BUB3 bound RZZ and co-eluted at a reduced elution volume. Conversely, mutants carrying

F475A, F500A-E501A, or their combination prevented binding in solution (**Fig. S4C-H**). Despite being paralogous to BUB1:BUB3, BUBR1:BUB3 did not bind RZZ (**Fig. S4I**). Thus, the BUB1 binding site for RZZ is bipartite, with two binding motifs that are both necessary, but individually insufficient, for a robust binding interaction *in vitro*. Confirming the importance of the first helix for MAD1 binding, both the F475A and the FFE mutants of $BUB1^{447-521}$, which share a dysfunctional first helix, showed little to no binding to MAD1:MAD2. The BUB1 FE mutant, however, had no impact on MAD1:MAD2 interaction, contrary to RZZ binding (**Fig. 3C-E**). In line with the crucial role of F475 in both MAD1 and RZZ binding, the previously described $BUB1^{RRK}$ mutant, where F475 is mutated together with two neighbouring residues (M474R, F475R, Q476K) (*43*), reduced both MAD1:MAD2 and RZZ binding to levels similar to those in the negative control (**Fig. S5A-D**).

Thus, RZZ interacts directly with a segment of BUB1 that is more extended of, but partly overlapping with, the one interacting with the $MAD1^{CTD}$. We used amber codon suppression technology (*49, 50*) to map the interaction of BUB1 with RZZ. Replacement of BUB1 residues F470 and I471 with the UV-photoactivatable crosslinker p-Benzoyl-L-phenylalanine (BPA) (**Fig. 3A**), followed by UV cross-linking, unequivocally indicated that $BUB1^{467-521}$ interacts with ROD (**Fig. 3F**).

Validation of the RZZ-binding site of BUB1 To validate the biological significance of these findings, we co-depleted endogenous BUB1 and CENP-E (**Fig. S6A-B**) in stable DLD-1 cell lines engineered to express various EGFP-BUB1 fusions, including $BUB1^{\Delta 467-521}$, $BUB1^{FFE}$, $BUB1^{F475A}$, $BUB1^{FE}$, and a construct containing only the BUB3 binding domain (GLEBS motif; $BUB1^{209-270}$) (**Fig. 3G** and **Fig. S6C**). In absence of transgene expression, RZZ and MAD1 were lost from kinetochores, as expected, whereas the levels of BUBR1 were only partially reduced (**Fig. 3H-I** and **Fig. S6H-I**). Expression of $BUB1^{FL}$ largely restored RZZ and MAD1 levels at prometaphase kinetochores (**Fig. 3H-I** and **Fig. S6D-F**). Instead, expression of $BUB1^{\Delta 467-521}$, $BUB1^{FFE}$, or $BUB1^{209-270}$ in cells depleted of BUB1 and CENP-E completely abrogated kinetochore recruitment of RZZ and MAD1 (**Fig. 3H-I** and **Fig. S6D-J**), whereas $BUB1^{F475A}$ and $BUB1^{FE}$ had intermediate effects, in line with the biochemical experiments. Because the kinetochore levels of BUBR1 were fully restored in presence of $BUB1^{FFE}$ (and of $BUB1^{F475A}$, or $BUB1^{FE}$) (**Fig. S6I**), our observations confirm that BUBR1 cannot replace BUB1 in RZZ or MAD1 recruitment when CENP-E is depleted.

Two BUB1-dependent axes of corona assembly Our studies identify two BUB1-dependent branches for RZZ recruitment, namely 1) a direct interaction of $BUB1^{467-521}$ with RZZ, and 2) an interaction of BUB1 with BUBR1 that in turn recruits CENP-E for RZZ binding. If correct, this model predicts that a BUB1 mutant impaired in its ability to recruit BUBR1-CENP-E and deleted of the 467-521 region that binds RZZ ought to be completely unable to recruit the RZZ. Indeed, a BUB1 mutant lacking residues 271-409 and 467-521 ($BUB1^{\Delta 271-409/467-521}$) caused complete

elimination of RZZ from kinetochores (**Fig. 4A-F**), while deletion of only the BUB1 helix ($BUB1^{\Delta 271-409}$) prevented BUBR1 recruitment but still supported robust RZZ localization (**Fig. 4A-F**). Kinetochore CENP-E was reduced in cells expressing $BUB1^{\Delta 271-409}$, and further reduced in cells expressing $BUB1^{\Delta 271-409/467-521}$, in agreement with the idea that BUBR1 and RZZS contribute to CENP-E recruitment.

To verify that the elusive kinetochore receptor of RZZ is indeed the binding site on BUB1 we have identified, we applied our stringent experiment with electroporated mCherry-tagged $R^{EE}ZZ$ in cells depleted of endogenous CENP-E and BUB1 and expressing either full-length $BUB1^{WT}$ or $BUB1^{FFE}$ transgenes (**Fig. 4G**). mCherry-$R^{EE}ZZ$ localized robustly to kinetochores in cells expressing $BUB1^{FL}$, but only minimal residual localization was observed in cells expressing $BUB1^{FFE}$ (**Fig. 4H-J**). Thus, when CENP-E depletion is coupled with mutations that prevent the interaction of BUB1 with RZZ, even constitutive polymerization in presence of endogenous MPS1 activity is insufficient for kinetochore recruitment of RZZS. Collectively, these findings provide a compelling recruitment model for the RZZ, as further discussed in Conclusions.

Cooperative binding of MAD1 and the RZZ to BUB1 An unexpected conundrum of our study concerns the MAD1 recruitment mechanism, as we have shown that the $MAD1^{CTD}$ and the RZZ compete for BUB1 binding. In principle, this problem may be solved by mobilizing a higher proportion of BUB1 than the sum of MAD1 and RZZ, thus buffering the effects of competition. This is a concrete possibility considering the relative cellular concentrations of these species and the fact that KNL1 exposes numerous MELT repeats to increase the multiplicity of BUB1 (*30, 51-57*). Nevertheless, a model purely based on competition seems unsatisfactory, as it would defy previous observations that RZZ facilitates MAD1 recruitment, rather than opposing it (*6, 26, 37, 39, 41, 42, 45, 58-63*). To shed further light on this question, we depleted BUB1 and CENP-E to eliminate MAD1 and RZZS. Re-expression of a $BUB1^{WT}$ transgene largely restored kinetochore MAD1. Albeit at reduced levels, re-expression of $BUB1^{S459-T461A}$, a mutant form of BUB1 that binds RZZ but not MAD1, also restored high levels of kinetochore MAD1 (**Fig. S7A-C**), confirming a role of RZZS in MAD1 recruitment downstream of BUB1.

To assess if RZZ binds MAD1:MAD2 directly, we polymerized RZZS into rings, as described previously (*9*) (**Fig. S7D**) and performed a pelleting assay with $BUB1^{467-521}$ and full-length MAD1:MAD2. MAD1:MAD2 and $BUB1^{467-521}$ pelleted with RZZS, while in absence of RZZS both proteins were almost entirely in the supernatant (**Fig. 5A**). As expected, $MAD1^{CTD}$, which competes with RZZ for BUB1 binding, was instead found in the supernatant (**Fig. 5A**). In another set of experiments, we titrated increasing amounts of MAD1:MAD2 (0.5-8 μM) and RZZ (0.5-8 μM) in presence of BUB1 as bait (at 8 μM). We observed a stepwise increase in bound proteins until both components reached apparently equimolar concentrations (**Fig. 5B** and **Fig. S7E-F**). This experiment indicates unequivocally that despite the apparent competition of the $MAD1^{CTD}$ and RZZ for BUB1, a MAD1 binding site on RZZ allows MAD1 to scale with RZZ on the BUB1 bait.

235 ***Conclusions*** We have dissected the molecular basis of kinetochore recruitment of the kinetochore corona, an essential part of the kinetochore scaffold in early mitosis. The recruitment pathway has its basis in the BUB1:BUBR1 complex of paralogous proteins, whose functional specialization from an original singleton represents a stunning example of molecular evolution (*31, 33, 64*). The pathway consists of two branches. The first branch uses BUB1 as a direct receptor through a
240 binding site on ROD. The second branch uses CENP-E, through BUBR1, which docks on BUB1 (*31, 36*). CENP-E interacts directly with an unknown binding site on the RZZ (*13*). While the two branches seem largely redundant for RZZS localization, we suspect them to be inseparable for proper corona function, as both contribute to robust localization of DD (*65*).

BUB1 lies at the fulcrum of the recruitment pathway. BUB1 is recruited largely through MPS1-
245 dependent phosphorylation of the MELT repeats on KNL1, so that MPS1 inhibition reduces BUB1 kinetochore binding. $R^{EE}ZZ$ bypasses the requirement of MPS1 kinase for kinetochore localization when CENP-E has been depleted (*13*). Likely, this is not due to an increase in binding affinity of $R^{EE}ZZ$ for BUB1, as RZZ^{WT}, $R^{AA}ZZ$ (the non-phosphorylatable mutant of RZZ), or $R^{EE}ZZ$ bound BUB1 with similar affinity in solid-phase or in solution (**Fig. S4H** and **Fig. S7G-H**). As $R^{EE}ZZ$
250 polymerizes when MPS1 is inhibited, its retention on CENP-E-depleted kinetochores indicates that it sticks more strongly than RZZ monomers to the residual BUB1. This is because monomers may be expected to require at least one corresponding BUB1 receptor for kinetochore recruitment, whereas a multivalent polymer may continue to bind even if only a handful of residual BUB1 remained after MPS1 inhibition (**Fig. 5C**). Thus, polymerization of the corona provides an
255 extremely robust, cooperative mechanism to retain attachment to kinetochores, making it resilient to temporary changes in local phosphorylation patterns and to progressive depletion of binding sites as microtubule attachment proceeds. Residual BUB1 levels due to incomplete depletions, and/or ectopic binding of BUBR1/BUB3 to MELT repeats after depletion of BUB1 (*31, 33, 66*), both causing substantial residual RZZ docking, likely explain why previous analyses of the role of
260 BUB1 in RZZ assembly in human cells led to conflicting conclusions (*26, 36-41*). Our observations also argue that BUB1, when bound to RZZ, is unlikely to satisfy a role as MAD1:MAD2 receptor. We surmise therefore that MAD1:MAD2 complexes recruited to RZZ interact with RZZ-free BUB1 molecules, which likely are numerous given the abundance of MELT repeats on KNL1 (**Fig. 5D**).

265 The physical interaction network of the corona integrates SAC and biorientation. By recruiting DD and CENP-E, the corona promotes transport of chromosomes to the spindle equator. By recruiting MAD1:MAD2, the corona promotes SAC signaling. The same mechanisms are also relevant for SAC silencing upon end-on conversion of microtubule attachment. This conversion detaches the chromosome cargo from the corona, activates DD, and allows corona disassembly,
270 removing MAD1:MAD2 from the kinetochore and causing its suppression, which turns off the SAC. Suppression of MPS1 activity, which in turn responds to Aurora B kinase, a master regulator of biorientation, is key to SAC silencing. Progressive suppression of MPS1 causes progressive dephosphorylation of the MELT repeats and of MAD1:MAD2 binding to BUB1, and directly

inactivates MAD1:MAD2 (*67, 68*). A crucial unresolved problem for future analyses is therefore how end-on conversion of microtubule attachment changes the inner fabric of interactions within the corona to allow DD activation and the transition to SAC silencing.

References

1. I. M. Cheeseman, A. Desai, Molecular architecture of the kinetochore-microtubule interface. *Nature reviews. Molecular cell biology* **9**, 33-46 (2008).
2. A. Musacchio, A. Desai, A Molecular View of Kinetochore Assembly and Function. *Biology (Basel)* **6**, (2017).
3. G. Kops, R. Gassmann, Crowning the Kinetochore: The Fibrous Corona in Chromosome Segregation. *Trends Cell Biol* **30**, 653-667 (2020).
4. B. Craske, J. P. Welburn, Leaving no-one behind: how CENP-E facilitates chromosome alignment. *Essays in biochemistry* **64**, 313-324 (2020).
5. A. D. McAinsh, G. Kops, Principles and dynamics of spindle assembly checkpoint signalling. *Nature reviews. Molecular cell biology*, (2023).
6. D. B. Hoffman, C. G. Pearson, T. J. Yen, B. J. Howell, E. D. Salmon, Microtubule-dependent changes in assembly of microtubule motor proteins and mitotic spindle checkpoint proteins at PtK1 kinetochores. *Molecular biology of the cell* **12**, 1995-2009 (2001).
7. R. Basto *et al.*, In vivo dynamics of the rough deal checkpoint protein during Drosophila mitosis. *Current biology : CB* **14**, 56-61 (2004).
8. E. Wojcik *et al.*, Kinetochore dynein: its dynamics and role in the transport of the Rough deal checkpoint protein. *Nature cell biology* **3**, 1001-1007 (2001).
9. T. Raisch *et al.*, Structure of the RZZ complex and molecular basis of Spindly-driven corona assembly at human kinetochores. *The EMBO journal* **41**, e110411 (2022).
10. J. A. Rodriguez-Rodriguez *et al.*, Distinct Roles of RZZ and Bub1-KNL1 in Mitotic Checkpoint Signaling and Kinetochore Expansion. *Current biology : CB* **28**, 3422-3429 e3425 (2018).
11. C. Sacristan *et al.*, Dynamic kinetochore size regulation promotes microtubule capture and chromosome biorientation in mitosis. *Nature cell biology* **20**, 800-810 (2018).
12. S. Santaguida, A. Tighe, A. M. D'Alise, S. S. Taylor, A. Musacchio, Dissecting the role of MPS1 in chromosome biorientation and the spindle checkpoint through the small molecule inhibitor reversine. *The Journal of cell biology* **190**, 73-87 (2010).
13. V. Cmentowski *et al.*, RZZ-Spindly and CENP-E form an integrated platform to recruit dynein to the kinetochore corona. *The EMBO journal* **42**, e114838 (2023).
14. J. Weber *et al.*, A conserved CENP-E region mediates BubR1-independent recruitment to the outer corona at mitotic onset. *Current Biology* **34**, 1133-1141. e1134 (2024).
15. J. Wu *et al.*, A farnesyl-dependent structural role for CENP-E in expansion of the fibrous corona. *Journal of Cell Biology* **223**, e202303007 (2023).
16. S. Eibes *et al.*, CENP-E activation by Aurora A and B controls kinetochore fibrous corona disassembly. *Nature communications* **14**, 5317 (2023).
17. S. Polley *et al.*, Structure of the human KMN complex and implications for regulation of its assembly. *Nature structural & molecular biology*, 1-13 (2024).
18. S. Martin-Lluesma, V. M. Stucke, E. A. Nigg, Role of Hec1 in spindle checkpoint signaling and kinetochore recruitment of Mad1/Mad2. *Science* **297**, 2267-2270 (2002).

19. V. M. Stucke, C. Baumann, E. A. Nigg, Kinetochore localization and microtubule interaction of the human spindle checkpoint kinase Mps1. *Chromosoma* **113**, 1-15 (2004).
20. Y. Hiruma *et al.*, CELL DIVISION CYCLE. Competition between MPS1 and microtubules at kinetochores regulates spindle checkpoint signaling. *Science* **348**, 1264-1267 (2015).
21. Z. Ji, H. Gao, H. Yu, CELL DIVISION CYCLE. Kinetochore attachment sensed by competitive Mps1 and microtubule binding to Ndc80C. *Science* **348**, 1260-1264 (2015).
22. T. Kiyomitsu, C. Obuse, M. Yanagida, Human Blinkin/AF15q14 is required for chromosome alignment and the mitotic checkpoint through direct interaction with Bub1 and BubR1. *Developmental cell* **13**, 663-676 (2007).
23. C. Pagliuca, V. M. Draviam, E. Marco, P. K. Sorger, P. De Wulf, Roles for the conserved spc105p/kre28p complex in kinetochore-microtubule binding and the spindle assembly checkpoint. *PLoS One* **4**, e7640 (2009).
24. L. A. Shepperd *et al.*, Phosphodependent recruitment of Bub1 and Bub3 to Spc7/KNL1 by Mph1 kinase maintains the spindle checkpoint. *Current biology : CB* **22**, 891-899 (2012).
25. C. Pereira *et al.*, Self-Assembly of the RZZ Complex into Filaments Drives Kinetochore Expansion in the Absence of Microtubule Attachment. *Current biology : CB* **28**, 3408-3421 e3408 (2018).
26. V. Silio, A. D. McAinsh, J. B. Millar, KNL1-Bubs and RZZ Provide Two Separable Pathways for Checkpoint Activation at Human Kinetochores. *Developmental cell* **35**, 600-613 (2015).
27. I. Primorac *et al.*, Bub3 reads phosphorylated MELT repeats to promote spindle assembly checkpoint signaling. *Elife* **2**, e01030 (2013).
28. Y. Yamagishi, C. H. Yang, Y. Tanno, Y. Watanabe, MPS1/Mph1 phosphorylates the kinetochore protein KNL1/Spc7 to recruit SAC components. *Nature cell biology* **14**, 746-752 (2012).
29. N. London, S. Ceto, J. A. Ranish, S. Biggins, Phosphoregulation of Spc105 by Mps1 and PP1 regulates Bub1 localization to kinetochores. *Current biology : CB* **22**, 900-906 (2012).
30. M. Vleugel *et al.*, Arrayed BUB recruitment modules in the kinetochore scaffold KNL1 promote accurate chromosome segregation. *The Journal of cell biology* **203**, 943-955 (2013).
31. K. Overlack *et al.*, A molecular basis for the differential roles of Bub1 and BubR1 in the spindle assembly checkpoint. *Elife* **4**, e05269 (2015).
32. R. Pleuger *et al.*, Microtubule end-on attachment maturation regulates Mps1 association with its kinetochore receptor. *Current biology : CB* **34**, 2279-2293 e2276 (2024).
33. K. Overlack *et al.*, BubR1 promotes Bub3-dependent APC/C inhibition during spindle assembly checkpoint signaling. *Current Biology* **27**, 2915-2927. e2917 (2017).
34. S. Jema *et al.*, Signaling protein abundance modulates the strength of the spindle assembly checkpoint. *Curr Biol* **33**, 4505-4515 e4504 (2023).
35. F. Edwards, G. Maton, N. Gareil, J. C. Canman, J. Dumont, BUB-1 promotes amphitelic chromosome biorientation via multiple activities at the kinetochore. *Elife* **7**, (2018).
36. G. Zhang, T. Lischetti, D. G. Hayward, J. Nilsson, Distinct domains in Bub1 localize RZZ and BubR1 to kinetochores to regulate the checkpoint. *Nature communications* **6**, 7162 (2015).
37. G. V. Caldas *et al.*, The RZZ complex requires the N-terminus of KNL1 to mediate optimal Mad1 kinetochore localization in human cells. *Open biology* **5**, (2015).
38. V. L. Johnson, M. I. Scott, S. V. Holt, D. Hussein, S. S. Taylor, Bub1 is required for kinetochore localization of BubR1, Cenp-E, Cenp-F and Mad2, and chromosome congression. *Journal of cell science* **117**, 1577-1589 (2004).

39. M. Vleugel *et al.*, Dissecting the roles of human BUB1 in the spindle assembly checkpoint. *Journal of cell science*, (2015).
40. C. Klebig, D. Korinth, P. Meraldi, Bub1 regulates chromosome segregation in a kinetochore-independent manner. *The Journal of cell biology* **185**, 841-858 (2009).
41. J. Qian *et al.*, An Attachment-Independent Biochemical Timer of the Spindle Assembly Checkpoint. *Molecular cell* **68**, 715-730 e715 (2017).
42. G. Ciossani *et al.*, The kinetochore proteins CENP-E and CENP-F directly and specifically interact with distinct BUB mitotic checkpoint Ser/Thr kinases. *The Journal of biological chemistry* **293**, 10084-10101 (2018).
43. E. S. Fischer *et al.*, Molecular mechanism of Mad1 kinetochore targeting by phosphorylated Bub1. *EMBO reports* **22**, e52242 (2021).
44. G. Zhang *et al.*, Bub1 positions Mad1 close to KNL1 MELT repeats to promote checkpoint signalling. *Nature communications* **8**, 15822 (2017).
45. S. Kim, H. Sun, D. R. Tomchick, H. Yu, X. Luo, Structure of human Mad1 C-terminal domain reveals its involvement in kinetochore targeting. *Proceedings of the National Academy of Sciences* **109**, 6549-6554 (2012).
46. J. A. Raaijmakers *et al.*, BUB1 Is Essential for the Viability of Human Cells in which the Spindle Assembly Checkpoint Is Compromised. *Cell Rep* **22**, 1424-1438 (2018).
47. Z. Ji, H. Gao, L. Jia, B. Li, H. Yu, A sequential multi-target Mps1 phosphorylation cascade promotes spindle checkpoint signaling. *Elife* **6**, e22513 (2017).
48. J. Jumper *et al.*, Highly accurate protein structure prediction with AlphaFold. *Nature* **596**, 583-589 (2021).
49. H. w. Ai, W. Shen, A. Sagi, P. R. Chen, P. G. Schultz, Probing Protein–Protein Interactions with a Genetically Encoded Photo-crosslinking Amino Acid. *Chembiochem* **12**, 1854 (2011).
50. L. Davis, J. W. Chin, Designer proteins: applications of genetic code expansion in cell biology. *Nature reviews Molecular cell biology* **13**, 168-182 (2012).
51. B. J. Howell *et al.*, Spindle checkpoint protein dynamics at kinetochores in living cells. *Current biology* **14**, 953-964 (2004).
52. Z. Tang, R. Bharadwaj, B. Li, H. Yu, Mad2-Independent inhibition of APCCdc20 by the mitotic checkpoint protein BubR1. *Developmental cell* **1**, 227-237 (2001).
53. V. Sudakin, G. K. Chan, T. J. Yen, Checkpoint inhibition of the APC/C in HeLa cells is mediated by a complex of BUBR1, BUB3, CDC20, and MAD2. *The Journal of cell biology* **154**, 925-936 (2001).
54. G. Fang, Checkpoint protein BubR1 acts synergistically with Mad2 to inhibit anaphase-promoting complex. *Molecular biology of the cell* **13**, 755-766 (2002).
55. X. Luo *et al.*, The Mad2 spindle checkpoint protein has two distinct natively folded states. *Nature structural & molecular biology* **11**, 338-345 (2004).
56. J. V. Shah *et al.*, Dynamics of centromere and kinetochore proteins; implications for checkpoint signaling and silencing. *Current biology : CB* **14**, 942-952 (2004).
57. B. J. Howell, D. B. Hoffman, G. Fang, A. W. Murray, E. D. Salmon, Visualization of Mad2 dynamics at kinetochores, along spindle fibers, and at spindle poles in living cells. *The Journal of cell biology* **150**, 1233-1250 (2000).
58. E. Buffin, C. Lefebvre, J. Huang, M. E. Gagou, R. E. Karess, Recruitment of Mad2 to the kinetochore requires the Rod/Zw10 complex. *Current biology : CB* **15**, 856-861 (2005).
59. G. J. Kops *et al.*, ZW10 links mitotic checkpoint signaling to the structural kinetochore. *The Journal of cell biology* **169**, 49-60 (2005).

60. R. Gassmann *et al.*, A new mechanism controlling kinetochore-microtubule interactions revealed by comparison of two dynein-targeting components: SPDL-1 and the Rod/Zwilch/Zw10 complex. *Genes & development* **22**, 2385-2399 (2008).
61. T. Alfonso-Perez, D. Hayward, J. Holder, U. Gruneberg, F. A. Barr, MAD1-dependent recruitment of CDK1-CCNB1 to kinetochores promotes spindle checkpoint signaling. *The Journal of cell biology* **218**, 1108-1117 (2019).
62. L. A. Allan *et al.*, Cyclin B1 scaffolds MAD1 at the kinetochore corona to activate the mitotic checkpoint. *The EMBO journal* **39**, e103180 (2020).
63. M. Jackman *et al.*, Cyclin B1-Cdk1 facilitates MAD1 release from the nuclear pore to ensure a robust spindle checkpoint. *The Journal of cell biology* **219**, (2020).
64. S. J. Suijkerbuijk *et al.*, The vertebrate mitotic checkpoint protein BUBR1 is an unusual pseudokinase. *Developmental cell* **22**, 1321-1329 (2012).
65. R. Gassmann, Dynein at the kinetochore. *Journal of cell science* **136**, (2023).
66. G. Zhang, B. L. Mendez, G. G. Sedgwick, J. Nilsson, Two functionally distinct kinetochore pools of BubR1 ensure accurate chromosome segregation. *Nature communications* **7**, 12256 (2016).
67. E. S. Fischer, Kinetochore-catalyzed MCC formation: a structural perspective. *IUBMB life* **75**, 289-310 (2023).
68. P. Lara-Gonzalez, J. Pines, A. Desai, Spindle assembly checkpoint activation and silencing at kinetochores. *Semin Cell Dev Biol* **117**, 86-98 (2021).

Acknowledgements: We thank Sabine Wohlgemuth for protein purifications.

Funding: This work was supported by the Max Planck Society (A.M.), the European Research Council (synergy grant 951430 BIOMECANET to A.M.), the Marie-Curie Training Network (DivIDE project number 675737 to A.M.), the German Research Foundation (DGF Collaborative Research Centre grant 1430 “Molecular Mechanisms of Cell State Transitions” to A.M.), and the CANTAR network under the Netzwerke-NRW program (A.M.).

Author contributions: Conceptualization: A.M., V.C.; Investigation: V.C.; Funding acquisition: A.M.; Project Administration: A.M.; Supervision: A.M. Validation: A.M., V.C.; Visualization: V.C., A.M; Writing – original draft: A.M., V.C.

Competing interests: Authors declare that they have no competing interests.

Data and materials availability: All data are available in the main text or the supplementary materials.

Supplementary Materials

Materials and Methods

Figures S1 to S7

455 Tables S1 to S3

References for Supplementary

Figure Legends:

Fig. 1. KNL1 promotes corona recruitment. (**A**) Graphical depiction of MPS1-phosphorylation-
460 dependent polymerization of RZZS. (**B**) Representative images showing localization of electroporated mCherry-RZZ^{WT} or mCherry-R^{EE}ZZ in cells treated with CENP-E RNAi. Before fixation, cells were synchronized in G2 phase with RO3306 for 15 h and then released into mitosis. Subsequently, cells were immediately treated with 3.3 µM nocodazole, 10 µM MG132, and 500 nM Reversine for an additional hour. CENP-C was used to visualize kinetochores. Scale bar: 5
465 µm. The experiment was performed three times. (**C**) Organization of outer kinetochore. Each straight line represents a different protein or protein complex. Gray circles represent direct protein interactions. Residues highlighted in yellow are phosphorylated by MPS1. Bypass conditions identified in (B) reveal existence of a second RZZ receptor. (**D**) Scheme for cell synchronization and RNAi treatment for the experiment shown in (E). (**E**) Representative images showing
470 localization of Zwilch in cells electroporated with mCherry-R^{EE}ZZ treated for RNAi as indicated and according to the scheme in panel (D). CENP-C was used to visualize kinetochores. Scale bar: 5 µm (**F-G**) Quantification of Zwilch levels at kinetochores of the experiment shown in (E). Red bars represent median (value shown above scatter dot plot) and interquartile range of normalized kinetochore intensity values. n refers to individually measured kinetochores (F left to right: 646,
475 459, 714, 814, G left to right: 469, 574, 641, 805) from two independent experiments. (**H**) Scheme of the MPS1-dependend recruitment of BUB1/BUB3 and BUBR1/BUB3 to the KNL1 constructs used in the experiment shown in (I). (**I**) Representative images showing the localization of Zwilch in stable DLD-1 cell lines expressing different KNL1 constructs. 24 h after cells were seeded and KNL1 as well as CENP-E were depleted, protein expression was induced through addition of
480 doxycycline and cells were synchronized in G2 phase with RO3306 for 15 h. Subsequently, cells were released into mitosis and immediately treated with 3.3 µM nocodazole, 10 µM MG132 and doxycycline for one hour before fixation. CENP-C was used to visualize kinetochores and DAPI to stain DNA. Scale bar: 5 µm. The experiment was performed three times.

485 **Fig. 2. RZZ and MAD1 bind directly to an overlapping region of BUB1.** (**A**) Scheme of BUB1 with relevant functional domains. (**B**) Quantification of Zwilch levels at kinetochores of DLD-1 cells depleted either for KNL1, CENP-E or BUB1 as indicated in the figure. 24 h after cells were seeded and treated with siRNA oligos cells were synchronized in G2 phase with 9 µM RO3306 for 15 h. Subsequently, cells were released into mitosis and immediately treated with 3.3 µM
490 nocodazole, 10 µM MG132 for one hour before fixation. Red bars represent median (value shown above scatter dot plot) and interquartile range of normalized kinetochore intensity values. n refers

to individually measured kinetochores (left to right: 662, 541, 748, 916, 803, 778) from two independent experiments. (**C**) Representative images showing the localization of Zwilch in stable DLD-1 cell lines expressing different BUB1 constructs. 24 h after cells were seeded and BUB1 as well as CENP-E were depleted, protein expression was induced through addition of doxycycline and cells were synchronized in G2 phase with RO3306 for 15 h. Subsequently, cells were released into mitosis and immediately treated with 3.3 µM nocodazole, 10 µM MG132 and doxycycline for one hour before fixation. CENP-C was used to visualize kinetochores and DAPI to stain DNA. Scale bar: 5 µm. The experiment was performed three times. (**D**) Crystal structure of $BUB1^{455-479}$ and $MAD1^{597-718}$ (adapted from Fischer et al., 2021; PDB: 7B1F). CDK1 and MPS1 phosphorylation sites are highlighted in red. (**E**) SDS-PAGE analysis of a pulldown assay with either GST or GST-tagged BUB1 constructs as bait and MBP-MAD1/2 as prey. For overnight phosphorylation bait and prey were incubated with CCC and $MPS1^{KD}$ for 16 h at 10˚C. Before SDS-PAGE analysis the eluate was dephosphorylated with λ-phosphatase for 30 mins at 25°C. (**F**) Quantification of the MAD1 band intensity normalized to the bait signal from the SDS-PAGE depicted in (E). The experiment was performed twice. (**G**) SDS-PAGE analysis of a pulldown assay with either GST or GST-tagged BUB1 constructs as bait, and mCherry-RZZ as prey. (**H**) Quantification of ROD band intensity normalized to the bait signal from the SDS-PAGE depicted in (G).

Fig. 3. Validation of the RZZ-binding site of BUB1. (**A**) Multiple sequence alignment showing the central domain of BUB1. Mutations discussed in main text are indicated above the sequence alignment. (**B**) AlphaFold2 prediction of $BUB1^{437-521}$. Amino acid substitutions are highlighted in black. (**C**) SDS-PAGE analysis of a pulldown assay with either GST or GST-tagged BUB1 baits, and mCherry-RZZ or MBP-MAD1/2 as prey. For overnight phosphorylation, bait and prey were incubated with CCC and $MPS1^{KD}$ for 16 h at 10˚C. Before SDS-PAGE analysis the eluate was dephosphorylated with λ-phosphatase for 30 mins at 25°C. (**D-E**) Quantification of the ROD and MAD1 band intensity normalized to the bait signal from the SDS-PAGE depicted in **c** from two individual repeats. (**F**) SDS-PAGE analysis of successful crosslinking of a $BUB1^{BPA}$ mutant with mCherry-RZZ upon treatment with UV light. The experiment was performed once. (**G**) Scheme for the cell synchronization and RNAi treatment for the experiment shown in (H). (**H**) Representative images showing the localization of Zwilch in stable DLD-1 cell lines expressing different BUB1 constructs treated as indicated in (G). CENP-C was used to visualize kinetochores and DAPI to stain DNA. Scale bar: 5 µm. (**I**) Quantification of Zwilch levels at kinetochores of the experiment shown in (H). Red bars represent median (value shown above scatter dot plot) and interquartile range of normalized kinetochore intensity values. n refers to individually measured kinetochores (left to right: 2423, 2033, 1152, 1016, 946, 980) from three independent experiments.

Fig. 4. BUB1 and BUBR1 paralogues recruit RZZ to the kinetochore. (**A**) Scheme of the stable DLD-1 cell lines used in the experiment depicted in (C). Cells expressed N-terminally EGFP-tagged BUB1 constructs upon addition of doxycycline. (**B**) Scheme for cell synchronization and RNAi treatment for the experiment shown in (C). (**C**) Representative images showing the

localization of Zwilch in stable DLD-1 cell lines expressing different BUB1 constructs treated as indicated in (B). CENP-C was used to visualize kinetochores and DAPI to stain DNA. Scale bar: 5 µm. (**D**) Quantification of Zwilch levels at kinetochores for experiment shown in (C). Red bars represent median (value shown above scatter dot plot) and interquartile range of normalized kinetochore intensity values. n refers to individually measured kinetochores (left to right: 304, 614, 362, 391). The experiment was performed three times. (**E**) Quantification of BUBR1 levels at kinetochores of the experiment shown in (C). Red bars represent median (value shown above scatter dot plot) and interquartile range of normalized kinetochore intensity values. n refers to individually measured kinetochores (left to right: 809, 825, 246, 464). The experiment was performed three times. (**F**) Quantification of CENP-E levels at kinetochores of the experiment shown in (C). Red bars represent median (value shown above scatter dot plot) and interquartile range of normalized kinetochore intensity values. n refers to individually measured kinetochores (left to right: 3672, 438, 504, 393). CENP-E staining was performed once. (**G**) Scheme of cell synchronization and RNAi treatment for the experiment shown in (H). (**H**) Representative images showing stable DLD-1 cell lines electroporated with mCherry-R^{EE}ZZ according to the experimental scheme shown in (G). CENP-C was used to visualize kinetochores and DAPI to stain DNA. Scale bar: 5 µm. (**I**) Least-square linear fitting of data points for each kinetochore of the mCherry intensity on the y-axis and the EGFP intensity on the x-axis of the experiment shown in (H). (**J**) Quantification of mCherry levels at kinetochores of the experiment shown in (H). Red bars represent median (value shown above scatter dot plot) and interquartile range of normalized kinetochore intensity values. n refers to individually measured kinetochores (left to right: 569, 620, 632, 657, 792, 658). The experiment was performed twice.

Fig. 5. Cooperative binding of MAD1 and the RZZ to BUB1. (**A**) SDS-PAGE analysis of a pelleting assay. mCherry-RZZ and GFP-$Spindly^{F}$ were polymerized overnight in presence of $MPS1^{KD}$ at 20°C. Subsequently, polymerized RZZS was incubated with BUB1 or MAD1 constructs for an additional 2 h at 20°C and finally applied to a glycerol cushion and spun in an ultracentrifuge. (**B**) SDS-PAGE analysis of a pulldown assay with either GST or GST-tagged BUB1 as bait, mCherry-RZZ (concentrations indicated) and MBP-MAD1:MAD2 (concentrations indicated) as prey. Phosphorylation bait and prey were incubated with CCC (CDK1:Cyclin B:CKS1) and $MPS1^{KD}$ for 16 h at 10˚C. Prior to SDS-PAGE analysis the eluate was dephosphorylated with λ-phosphatase for 30 mins at 25°C. (**C**) Scheme depicting RZZ recruitment to the kinetochore through interaction with BUB1. (**D**) Revised hierarchal organization of outer kinetochore and kinetochore corona based on our new results.

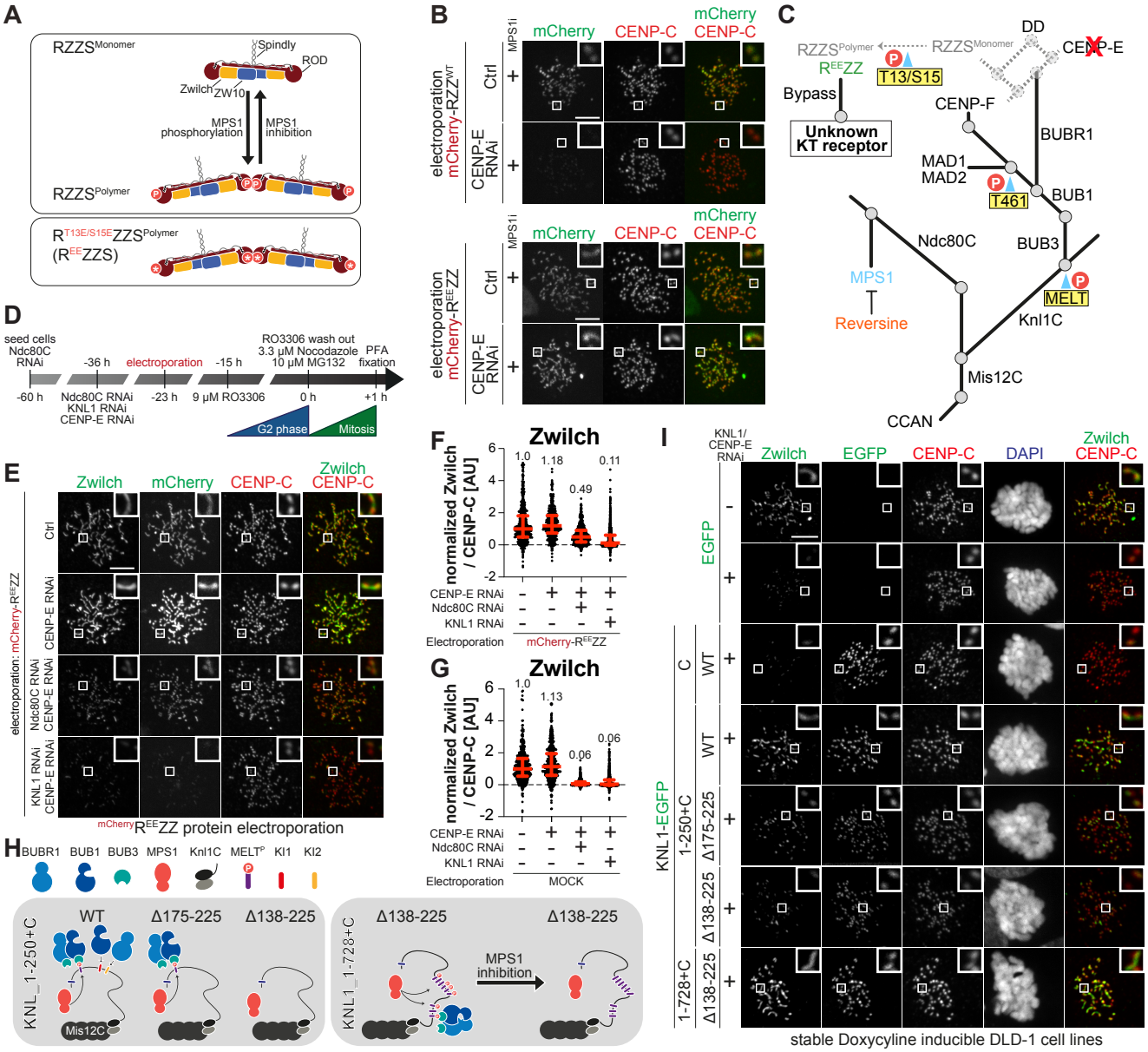
A
RZZS Monomer
Spindly
ROD
Zwilch
ZW10
MPS1 phosphorylation
MPS1 inhibition
RZZS Polymer
R T13E/S15E ZZS Polymer
(R EE ZZS)
B
MPS1i
mCherry
CENP-C
mCherry CENP-C
electroporation
mCherry-RZZ WT
mCherry-R EE ZZ
Ctrl
CENP-E RNAi
C
RZZS Polymer
R EE ZZ
T13/S15
RZZS Monomer
DD
CENP-E
Bypass
Unknown KT receptor
CENP-F
BUBR1
MAD1
MAD2
T461
BUB1
Ndc80C
BUB3
MPS1
Reversine
MELT
Knl1C
Mis12C
CCAN
D
seed cells
Ndc80C RNAi
-36 h
electroporation
-15 h
RO3306 wash out
3.3 μM Nocodazole
10 μM MG132
PFA fixation
-60 h
Ndc80C RNAi
KNL1 RNAi
CENP-E RNAi
-23 h
9 μM RO3306
0 h
+1 h
G2 phase
Mitosis
E
Zwilch
mCherry
CENP-C
Zwilch CENP-C
electroporation: mCherry-R EE ZZ
Ctrl
CENP-E RNAi
Ndc80C RNAi CENP-E RNAi
KNL1 RNAi CENP-E RNAi
mCherry R EE ZZ protein electroporation
F
Zwilch
normalized Zwilch / CENP-C [AU]
1.0
1.18
0.49
0.11
CENP-E RNAi
Ndc80C RNAi
KNL1 RNAi
Electroporation
mCherry-R EE ZZ
G
Zwilch
1.0
1.13
0.06
0.06
MOCK
H
BUBR1
BUB1
BUB3
MPS1
Knl1C
MELT P
KI1
KI2
KNL_1-250+C
WT
Δ175-225
Δ138-225
Mis12C
KNL1_1-728+C
Δ138-225
Δ138-225
MPS1 inhibition
I
KNL1/ CENP-E RNAi
Zwilch
EGFP
CENP-C
DAPI
Zwilch CENP-C
KNL1-EGFP
1-250+C
1-728+C
WT
Δ175-225
Δ138-225
stable Doxycyline inducible DLD-1 cell lines

Figure 1

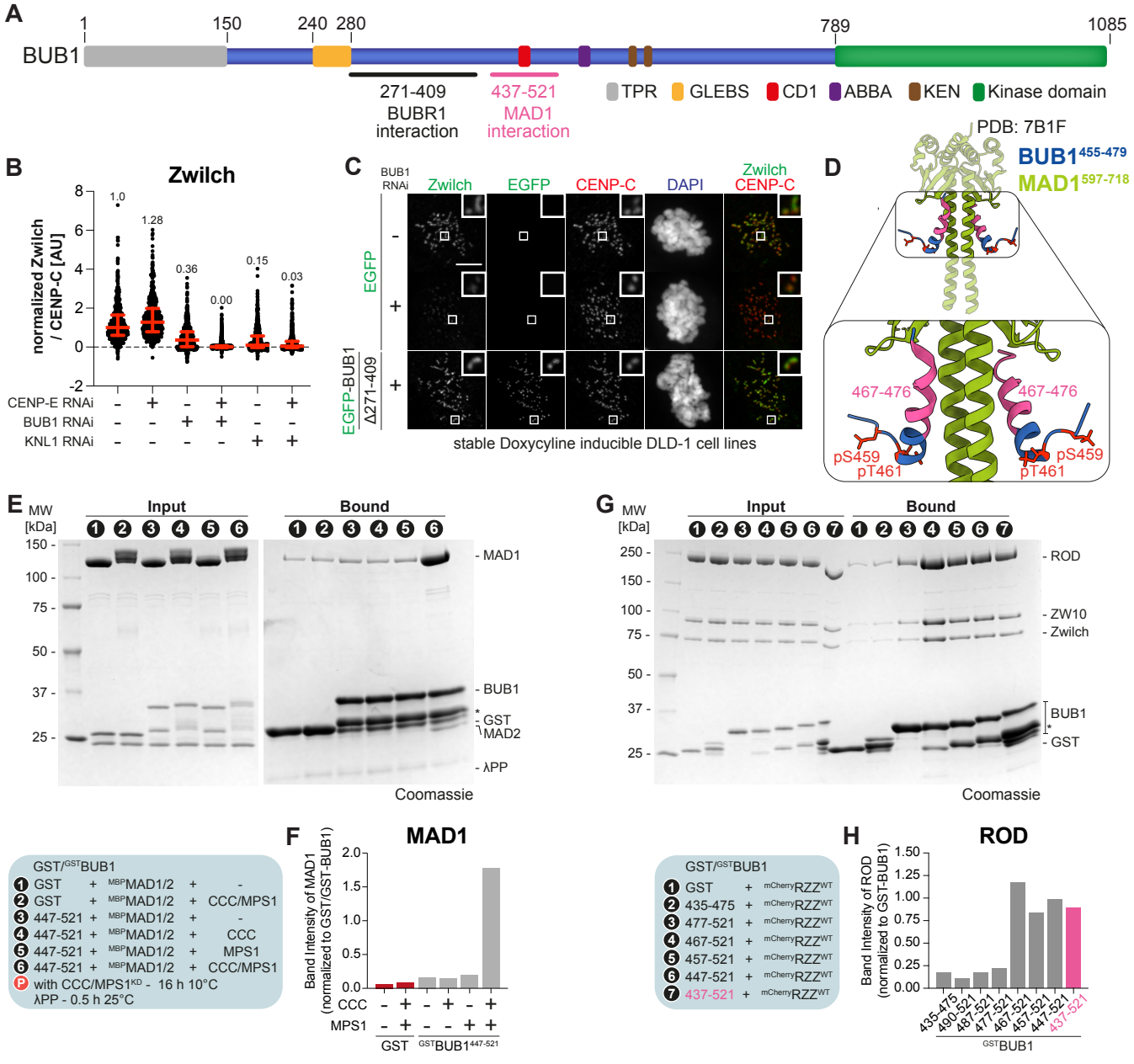
A
BUB1
1
150
240
280
789
1085
271-409
BUBR1
interaction
437-521
MAD1
interaction
TPR
GLEBS
CD1
ABBA
KEN
Kinase domain
B
Zwilch
normalized Zwilch / CENP-C [AU]
1.0
1.28
0.36
0.00
0.15
0.03
CENP-E RNAi
BUB1 RNAi
KNL1 RNAi
C
BUB1 RNAi
Zwilch
EGFP
CENP-C
DAPI
Zwilch CENP-C
EGFP
EGFP-BUB1 Δ271-409
stable Doxycycline inducible DLD-1 cell lines
D
PDB: 7B1F
BUB1455-479
MAD1597-718
467-476
467-476
pS459
pT461
pS459
pT461
E
MW [kDa]
Input
Bound
150
100
75
50
37
25
MAD1
BUB1
GST
MAD2
λPP
Coomassie
GST/GSTBUB1
1 GST + MBPMAD1/2 + -
2 GST + MBPMAD1/2 + CCC/MPS1
3 447-521 + MBPMAD1/2 + -
4 447-521 + MBPMAD1/2 + CCC
5 447-521 + MBPMAD1/2 + MPS1
6 447-521 + MBPMAD1/2 + CCC/MPS1
P with CCC/MPS1KD - 16 h 10°C
λPP - 0.5 h 25°C
F
MAD1
Band Intensity of MAD1 (normalized to GST/GST-BUB1)
2.0
1.5
1.0
0.5
0.0
CCC
MPS1
GST
GSTBUB1447-521
G
MW [kDa]
Input
Bound
250
150
100
75
50
37
25
ROD
ZW10
Zwilch
BUB1
GST
Coomassie
GST/GSTBUB1
1 GST + mCherryRZZWT
2 435-475 + mCherryRZZWT
3 477-521 + mCherryRZZWT
4 467-521 + mCherryRZZWT
5 457-521 + mCherryRZZWT
6 447-521 + mCherryRZZWT
7 437-521 + mCherryRZZWT
H
ROD
Band Intensity of ROD (normalized to GST-BUB1)
1.50
1.25
1.00
0.75
0.50
0.25
0.00
435-475
490-521
487-521
477-521
467-521
457-521
447-521
437-521
GSTBUB1

Figure 2

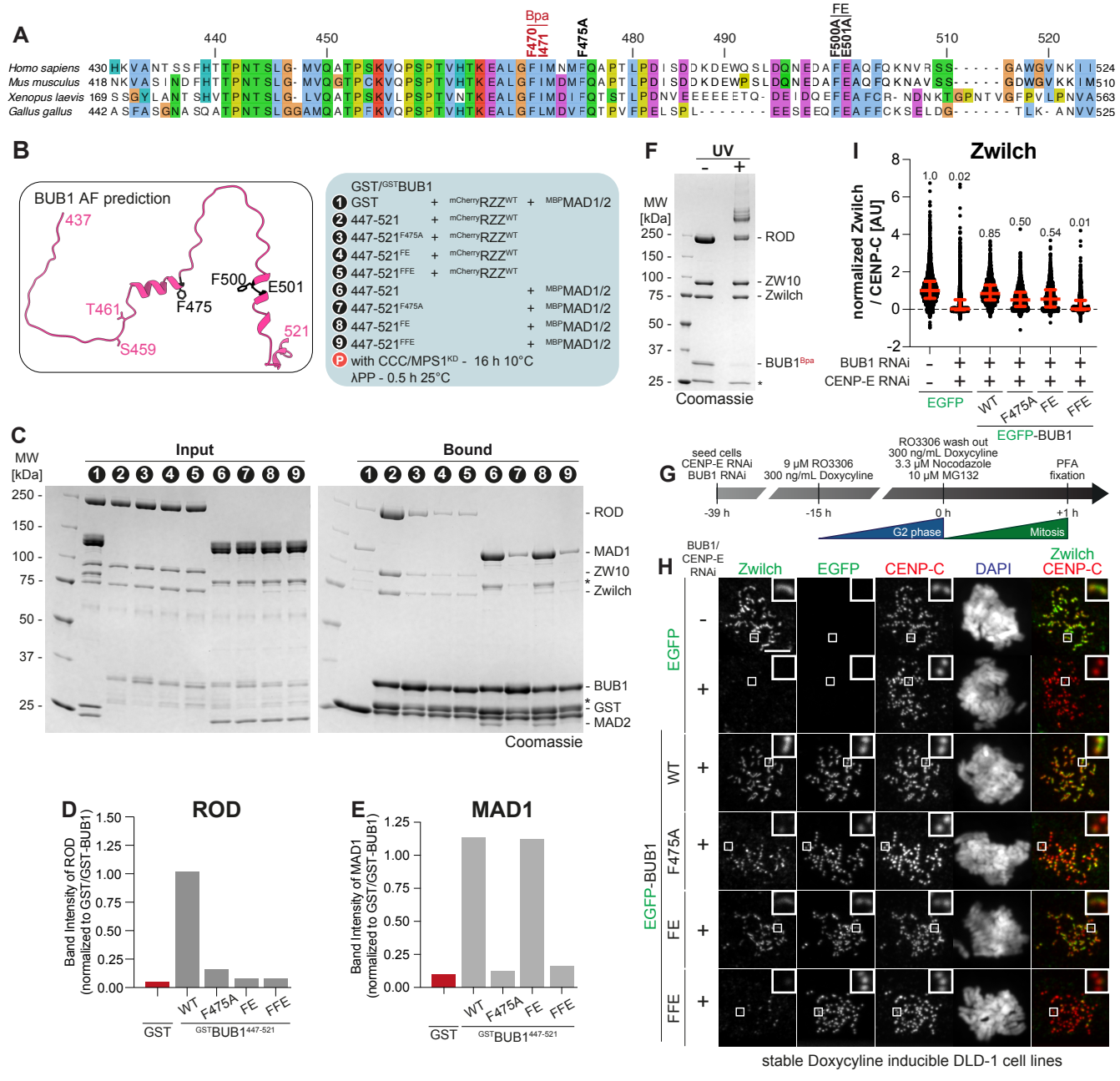
A
Bpa
F470
I471
F475A
FE
F500A
E501A
440
450
480
490
510
520
Homo sapiens 430 HKVANTSSFHTTPNTSLG- MVQATPSKVQPSPTVHTKEALGFIMNMFQAPTLPDISDDKDEWQSLDQNEDAFEAQFQKNVRSS- - - - - GAWGVNKII 524
Mus musculus 418 NKVASINDFHTTPNTSLG- MVQGTPCKVQPSPTVHTKEALGFIMDMFQAPTLPDISDDKDEWPSLDQNEDAFEAQFQKNAVSS- - - - - GDWGVKKIM 510
Xenopus laevis 169 SSGYLANTSHVTPNTSLG- LVQATPSKVLPSPTVNTKEALGFIMDIFQTSTLPDNVEEEEEETQ- DEIDQEFEAFCR- NDNKTGPNTVGFPVLPNVA 563
Gallus gallus 442 ASFASGNASQATPNTSLGGAMQATPFKVQPSPTVHTKEALGFLMDVFQTPVFPELSPL- - - - - - - EESEEQFEAFFCKSELDG- - - - - - TLK- ANVV 525
B
BUB1 AF prediction
437
T461
S459
F475
F500
E501
521
GST/GSTBUB1
1 GST + mCherryRZZWT + MBPMAD1/2
2 447-521 + mCherryRZZWT
3 447-521F475A + mCherryRZZWT
4 447-521FE + mCherryRZZWT
5 447-521FFE + mCherryRZZWT
6 447-521 + MBPMAD1/2
7 447-521F475A + MBPMAD1/2
8 447-521FE + MBPMAD1/2
9 447-521FFE + MBPMAD1/2
P with CCC/MPS1KD - 16 h 10°C
λPP - 0.5 h 25°C
F
UV
-
+
MW [kDa]
250 -
150 -
100 -
75 -
50 -
37 -
25 -
ROD
ZW10
Zwilch
BUB1Bpa
*
Coomassie
I
Zwilch
normalized Zwilch / CENP-C [AU]
8
6
4
2
0
-2
1.0
0.02
0.85
0.50
0.54
0.01
BUB1 RNAi - + + + + +
CENP-E RNAi - + + + + +
EGFP
WT
F475A
FE
FFE
EGFP-BUB1
C
MW [kDa]
Input
Bound
1 2 3 4 5 6 7 8 9
250 -
150 -
100 -
75 -
50 -
37 -
25 -
ROD
MAD1
ZW10
*
Zwilch
BUB1
*
GST
MAD2
Coomassie
G
seed cells
CENP-E RNAi
BUB1 RNAi
9 µM RO3306
300 ng/mL Doxycyline
RO3306 wash out
300 ng/mL Doxycyline
3.3 µM Nocodazole
10 µM MG132
PFA fixation
-39 h
-15 h
0 h
+1 h
G2 phase
Mitosis
H
BUB1/ CENP-E RNAi
Zwilch
EGFP
CENP-C
DAPI
Zwilch CENP-C
EGFP
-
+
EGFP-BUB1
WT
+
F475A
+
FE
+
FFE
+
stable Doxycyline inducible DLD-1 cell lines
D
ROD
Band Intensity of ROD (normalized to GST/GST-BUB1)
1.50
1.25
1.00
0.75
0.50
0.25
0.00
GST
WT
F475A
FE
FFE
GSTBUB1447-521
E
MAD1
Band Intensity of MAD1 (normalized to GST/GST-BUB1)
1.25
1.00
0.75
0.50
0.25
0.00
GST
WT
F475A
FE
FFE
GSTBUB1447-521

Figure 3

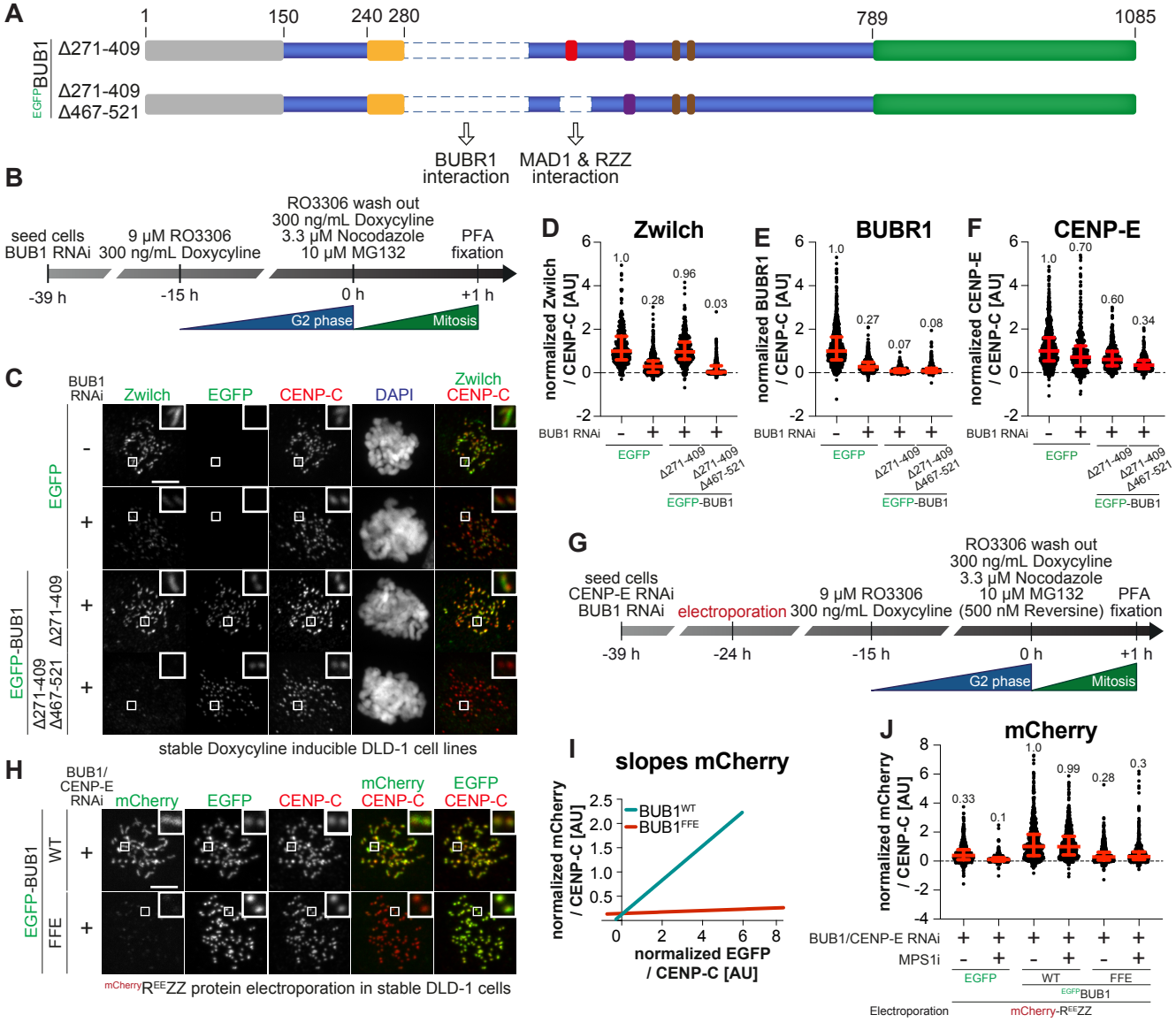
A
1
150
240 280
789
1085
EGFP BUB1
Δ271-409
Δ271-409
Δ467-521
BUBR1 interaction
MAD1 & RZZ interaction
B
seed cells
BUB1 RNAi
9 μM RO3306
300 ng/mL Doxycyline
RO3306 wash out
300 ng/mL Doxycyline
3.3 μM Nocodazole
10 μM MG132
PFA fixation
-39 h
-15 h
0 h
+1 h
G2 phase
Mitosis
C
BUB1 RNAi
Zwilch
EGFP
CENP-C
DAPI
Zwilch CENP-C
EGFP
EGFP-BUB1
Δ271-409
Δ271-409 Δ467-521
stable Doxycyline inducible DLD-1 cell lines
D
Zwilch
normalized Zwilch / CENP-C [AU]
1.0
0.28
0.96
0.03
BUB1 RNAi
EGFP
EGFP-BUB1
Δ271-409
Δ271-409 Δ467-521
E
BUBR1
normalized BUBR1 / CENP-C [AU]
1.0
0.27
0.07
0.08
F
CENP-E
normalized CENP-E / CENP-C [AU]
1.0
0.70
0.60
0.34
G
seed cells
CENP-E RNAi
BUB1 RNAi
electroporation
9 μM RO3306
300 ng/mL Doxycyline
RO3306 wash out
300 ng/mL Doxycyline
3.3 μM Nocodazole
10 μM MG132
(500 nM Reversine)
PFA fixation
-39 h
-24 h
-15 h
0 h
+1 h
G2 phase
Mitosis
H
BUB1/ CENP-E RNAi
mCherry
EGFP
CENP-C
mCherry CENP-C
EGFP CENP-C
EGFP-BUB1
WT
FFE
mCherry-REEZZ protein electroporation in stable DLD-1 cells
I
slopes mCherry
normalized mCherry / CENP-C [AU]
BUB1WT
BUB1FFE
normalized EGFP / CENP-C [AU]
J
mCherry
normalized mCherry / CENP-C [AU]
0.33
0.1
1.0
0.99
0.28
0.3
BUB1/CENP-E RNAi
MPS1i
EGFP
WT
FFE
EGFP-BUB1
Electroporation
mCherry-REEZZ

Figure 4

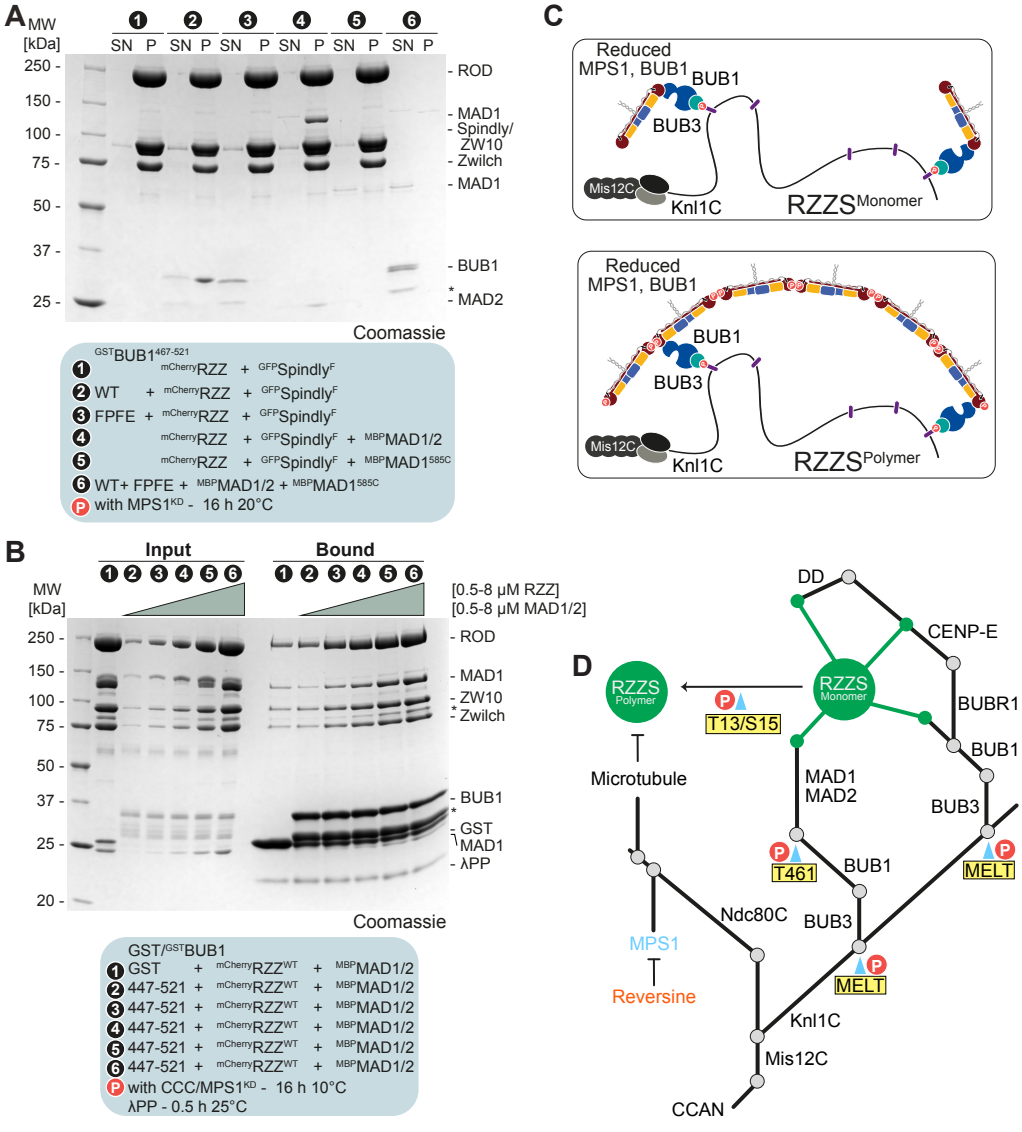
A
MW [kDa]
1 2 3 4 5 6
SN P SN P SN P SN P SN P SN P
250 -
150 -
100 -
75 -
50 -
37 -
25 -
- ROD
- MAD1
- Spindly/ ZW10
- Zwilch
- MAD1
- BUB1
* - MAD2
Coomassie
1 GSTBUB1467-521 mCherryRZZ + GFPSpindlyF
2 WT + mCherryRZZ + GFPSpindlyF
3 FPFE + mCherryRZZ + GFPSpindlyF
4 mCherryRZZ + GFPSpindlyF + MBPMAD1/2
5 mCherryRZZ + GFPSpindlyF + MBPMAD1585C
6 WT+ FPFE + MBPMAD1/2 + MBPMAD1585C
P with MPS1KD - 16 h 20°C
B
Input
Bound
1 2 3 4 5 6
1 2 3 4 5 6
MW [kDa]
[0.5-8 µM RZZ]
[0.5-8 µM MAD1/2]
250 -
150 -
100 -
75 -
50 -
37 -
25 -
20 -
- ROD
- MAD1
- ZW10
* - Zwilch
- BUB1
* - GST
- MAD1
- λPP
Coomassie
GST/GSTBUB1
1 GST + mCherryRZZWT + MBPMAD1/2
2 447-521 + mCherryRZZWT + MBPMAD1/2
3 447-521 + mCherryRZZWT + MBPMAD1/2
4 447-521 + mCherryRZZWT + MBPMAD1/2
5 447-521 + mCherryRZZWT + MBPMAD1/2
6 447-521 + mCherryRZZWT + MBPMAD1/2
P with CCC/MPS1KD - 16 h 10°C
λPP - 0.5 h 25°C
C
Reduced MPS1, BUB1
BUB1
BUB3
Mis12C
Knl1C
RZZSMonomer
Reduced MPS1, BUB1
BUB1
BUB3
Mis12C
Knl1C
RZZSPolymer
D
DD
CENP-E
RZZS Polymer
RZZS Monomer
P T13/S15
BUBR1
BUB1
Microtubule
MAD1
MAD2
BUB3
P T461
BUB1
P MELT
Ndc80C
BUB3
MPS1
P MELT
Reversine
Knl1C
Mis12C
CCAN

Figure 5